BNL-112684-2016-JA

Heterogeneous WSx/WO3 Thorn-Bush Nanofiber Electrodes for Sodium-Ion Batteries

Won-Hee Ryu, Hope Wilson, Sungwoo Sohn, Jinyang Li, Xiao Tong, Evyatar Shaulsky, Jan Schroers, Menachem Elimelech, and André D. Taylor

Submitted to the Journal of American Chemical Society

January, 2016

Center for Functional Nanomaterials

Brookhaven National Laboratory

U.S. Department of Energy
USDOE Office of Science (SC),
Basic Energy Sciences (BES) (SC-22)

DISCLAIMER

Heterogeneous WS_x/WO_3 Thorn-Bush Nanofiber Electrodes for Sodium-Ion Batteries

Won-Hee Ryu,[†,⊥] Hope Wilson,[†] Sungwoo Sohn,[‡] Jinyang Li,[†] Xiao Tong,[§] Evyatar Shaulsky,[†] Jan Schroers,[‡] Menachem Elimelech,[†] and André D. Taylor*[,†]

[†]Department of Chemical and Environmental Engineering, Yale University, 9 Hillhouse Avenue, New Haven, Connecticut 06511, United States

[‡]Department of Mechanical Engineering and Materials Science, Yale University, Prospect Street, New Haven, Connecticut 06511, United States

[§]Center for Functional Nanomaterials, Brookhaven National Laboratory, Upton, New York 11973, United States

Supporting Information

ABSTRACT: **Heterogeneous electrode materials with hierarchical architectures promise to enable considerable improvement in future energy storage devices. In this study, we report on a tailored synthetic strategy used to create heterogeneous tungsten sulfide/oxide core−shell nanofiber materials with vertically and randomly aligned thorn-bush features, and we evaluate them as potential anode materials for high-performance Na-ion batteries. The WS_x ($2 \leq x \leq 3$, amorphous WS_3 and crystalline WS_2) nanofiber is successfully prepared by electrospinning and subsequent calcination in a reducing atmosphere. To prevent capacity degradation of the WS_x anodes originating from sulfur dissolution, a facile post-thermal treatment in air is applied to form an oxide passivation surface. Interestingly, WO_3 thorn bundles are randomly grown on the nanofiber stem, resulting from the surface conversion. We elucidate the evolving morphological and structural features of the nanofibers during post-thermal treatment. The heterogeneous thorn-bush nanofiber electrodes deliver a high second discharge capacity of 791 mAh g^{-1} and improved cycle performance for 100 cycles compared to the pristine WS_x nanofiber. We show that this hierarchical design is effective in reducing sulfur dissolution, as shown by cycling analysis with counter Na electrodes.**

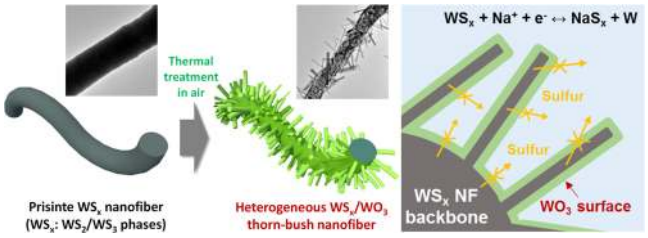

KEYWORDS: *sodium-ion batteries, electrospinning, tungsten sulfide, nanofiber, heterogeneous structure*

Recent energy storage trends are focusing on large-scale devices and systems such as electric vehicles, electricity storage devices for uninterruptible power systems, and parity matching for renewable energy devices on smart grids.[1,2] To meet the practical and economic criteria for large-scale systems, Na-ion batteries have been considered due to their beneficial aspects compared to conventional Li-ion batteries.[3−5] Efforts have been made to realize low-cost batteries by utilizing abundant and easily accessible Na resources. Further, the analogous structure and electrochemistry of Na-ion batteries to those of Li-ion batteries are particularly attractive, as they may allow application of a Na-ion setup to existing battery technologies.[6]

The performance of Na-ion batteries is mainly determined by the electrode materials, whose properties are influenced by their diverse composition and versatile morphological characteristics.[7,8] Due to the larger ionic radius of Na ions (1.06 Å) than that of Li ions (0.76 Å), conventional anode materials (*e.g.*, graphite, Si) for Li-ion batteries suffer from poor insertion/extraction kinetics with Na ions, thereby exhibiting lower capacity and insufficient cycling.[9,10] Alternatives such as nongraphitic carbon (*e.g.*, hard carbon and carbon spheres),[11−13] metal alloys (*e.g.*, Sn, Sb, P),[14−18] and intercalation compounds (*e.g.*, TiO_2 and $Na_2Ti_3O_7$)[19−21] have been considered to improve anode performance. Recently, a class of metal oxides (*e.g.*, CuO, Fe_2O_3), known as conversion reaction anodes, has been considered to capitalize on their complementary features of (i) higher Na capacity than carbons or intercalation anodes and (ii) better structural stability than metal alloys.[22−24] However, these metal oxides typically provide low capacity (<400 mAh/g) as representative conversion reaction anodes for Na-ion batteries.[25]

In this regard, metal sulfide materials have recently been considered as high capacity anode materials for Na-ion batteries because of (i) the large slab space between their 2-D planes, (ii) their reversible conversion reaction characteristics, and (iii) the

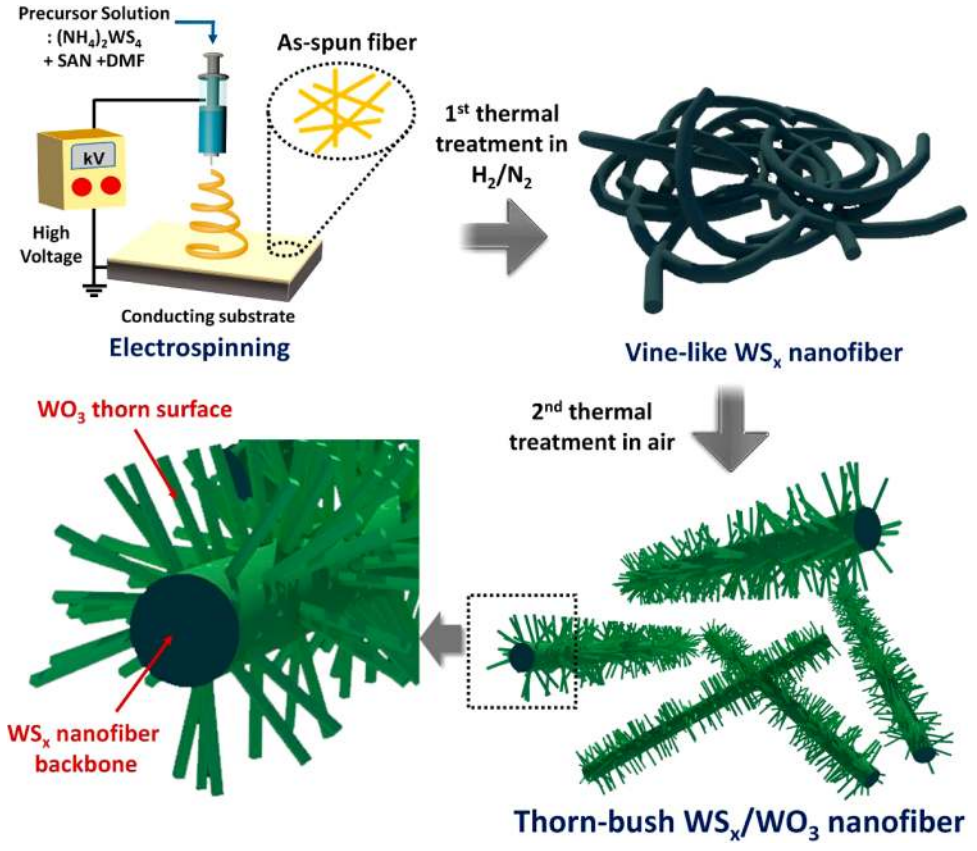

Figure 1. Schematic illustration of the synthetic strategy used to create the heterogeneous WS_x/WO_3 thorn-bush nanofibers.

higher conductivity of Na_2S products (metal sulfides) compared to Na_2O (metal oxides).[26−30] The metal disulfide (MS_2, M = Mo, W) reaction involves intercalation of sodium at the beginning and a subsequent conversion reaction ($MS_2 + 4Na^+ + 4e^- \rightarrow 2\ Na_2S + M$).[26,31] Similarly, amorphous metal trisulfides (MS_3, M = Mo, W) could be considered as high capacity anode materials due to the structural flexibility of their glassy phase and the excess sulfur as an active component ($MS_3 + 6Na^+ + 6e^- \rightarrow 3Na_2S + M$). Moreover, the electronic conductivity of MS_3 can be improved by excess sulfur in the sulfide structure.[32] To date, however, Na battery performance of MS_3 has not been thoroughly reported.

To further improve the kinetic performance of metal sulfide materials, reducing the size dimension to the nanoscale and tailoring their morphologies can afford an increased number of reaction sites and reduced Na-ion diffusion.[27,31,33,34] While metal sulfides deliver an improved capacity of >700 mAh/g, a solution is needed for the sulfur dissolution issue originating from soluble polysulfide intermediates during the Na_2S formation/decomposition process, thereby losing sulfur components and consequently degrading capacity.[26] The introduction of a protective layer on the surface could improve cyclability by preventing the dissolution of the intermediates and consequently the accumulation of the sulfur phase on the Na counter electrode.[26,35] Similarly, polysulfide shuttling in the Li−S battery system has been mitigated by encapsulating or covering the surface of the sulfur cathodes.[36−38] While the coating layers on the metal sulfide nanostructure have been applied by a postprocess utilizing carbon composite and metal oxide layers,[26,35] a facile and advanced coating process is preferred to precisely control the surface layer on the metal sulfide nanomaterials.

In this paper, we report heterogeneous tungsten sulfide (WS_x)/tungsten oxide (WO_3) core−shell composite materials with thorn-bush nanofiber (NF) structures for an improved Na-ion battery anode. WS_x ($2 < x < 3$) NFs composed of amorphous WS_3 and crystalline WS_2 phases are successfully synthesized by electrospinning of ammonium tetrathiotungstate ($(NH_4)_2WS_4$) and poly(styrene-acrylonitrile) (SAN) and subsequent calcination in a reducing atmosphere (Figure 1). A post-thermal treatment in air is then carried out to form metal oxide surfaces on the WS_x NFs. Interestingly, we observe an unexpected morphological change of vertical and random growth of WO_3 thorns on the NF surface, and we examine the structural and chemical evolution of these features after post-thermal treatment at different calcination temperatures. The electrochemical performance of the thorn-bush WS_x/WO_3 core−shell composite NFs is evaluated to assess their potential as anode materials for high-capacity and long-cycle Na-ion batteries. We also directly observe precipitated sulfurs on cycled Na counter electrodes to confirm the reduced degree of sulfur dissolution resulting from the metal oxide passivation surface. Our proposed facile fabrication strategy for heterogeneous nanostructures composed of tungsten sulfide and tungsten oxide have important implications for energy storage applications.

RESULTS AND DISCUSSION

Morphological Features. The one-dimensional (1-D) heterogeneous WS_x/WO_3 NFs can provide improved Na capacity and fast reaction kinetics for a reversible conversion

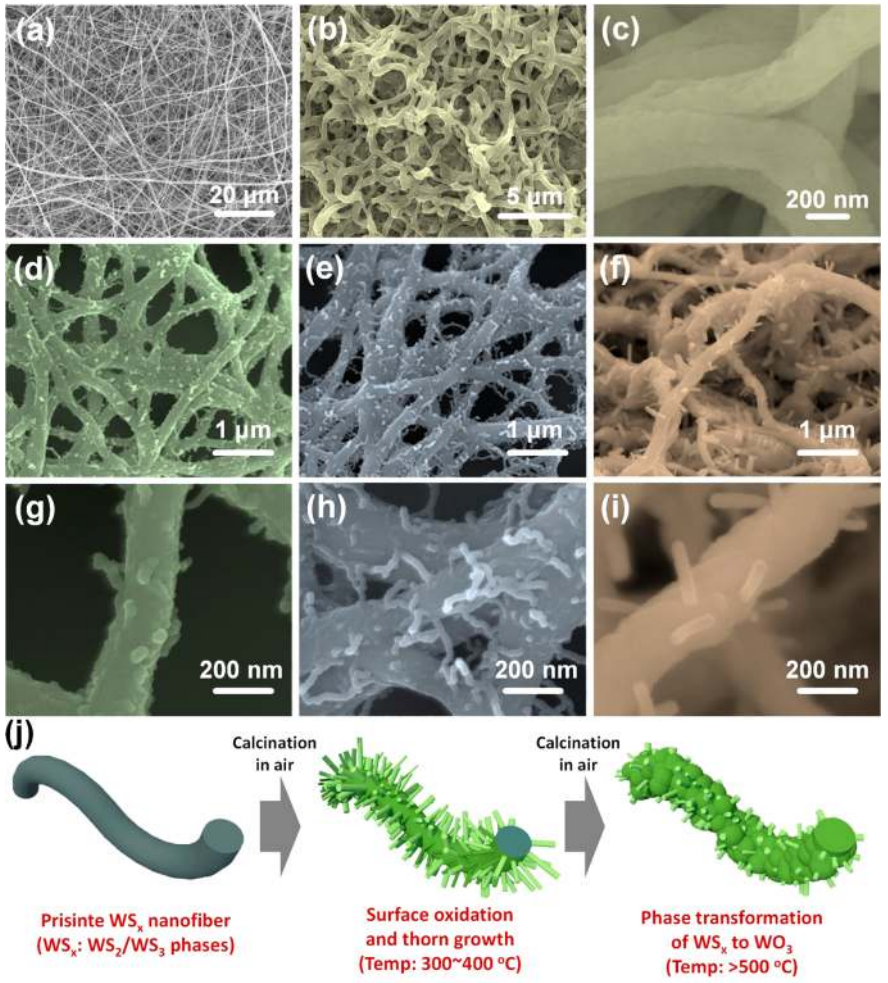

Figure 2. (a) SEM image of the as-spun composite nanofibers of $(NH_4)_2WS_4$ precursor with a SAN polymer prepared by electrospinning; (b, c) SEM images of WS_x nanofibers calcined at 700 °C for 6 h under a reducing atmosphere (H_2/N_2, 10%/90% v/v) at different magnification levels; SEM images of the postcalcined WS_x nanofibers in air at (d, g) 300 °C, (e, h) 400 °C, and (g, i) 500 °C collected at different magnification levels; (j) schematic diagrams of morphological evolutions of WS_x nanofibers during calcination in air.

reaction due to their unique morphological and chemical characteristics. We synthesized WS_x/WO_3 NF materials by electrospinning followed by subsequent thermal heat treatments under reducing (H_2/N_2, 10%/90% v/v) and air atmospheres. The morphological features of the NFs for a series of synthesis steps are presented in Figure 2. As-spun composite fibers of $(NH_4)_2WS_4$ and the SAN polymer exhibited a smooth surface and continuous features with an average diameter of 300 nm (Figure 2a and Figure S1). With increased heating times, the fiber shape became tangled and the fibers merged with each other by burning out the SAN polymer templates and forming crystalline structures from the $(NH_4)_2WS_4$ precursor (Figure 2b and c, Figure S2). We observe vine-like shapes after calcination at 700 °C for 6 h, which are related to the typical morphological features resulting from SAN polymer decomposition.[26] We show single NFs (diameter: 150−200 nm) and bundle diameters ranging from 300 to 500 nm (Figure 2c). The second heat treatment in air (~10 min) forms an oxide layer on the surface of the sulfide NFs (Figure 2d and e). Interestingly, nanobranches grow on the surface during the post-thermal treatment, and the length and density of these branches increase along with the calcination temperature from 300 to 400 °C (Figure 2g and h). The agglomerated bundles of pristine sulfide fibers became straight and separate during the partial conversion to the oxide phase. After calcination at 500 °C, which is known to be the oxide formation temperature, the thorn length decreases and crystalline grains appear (Figure 2f and i), indicating that a structural transformation and consequent morphological conversion occurs. Overall morphological evolution details during post-thermal treatment in air were summarized in Figure 2j.

Thermal Behaviors for First and Second Calcinations. The thermal behavior of the NFs during calcination was examined to explain the synthesis mechanism (Figure S3 and Figure 3a). First, we show thermogravimetric analysis (TGA)/differential scanning calorimetry (DSC) curves of the as-spun NFs with increasing temperature in H_2/N_2, corresponding to the first thermal treatment (Figure S3). For as-spun fibers, the first endothermic peak of the DSC curve at 205 °C is related to the decomposition of the $(NH_4)_2WS_4$ precursor and the formation of WS_x phases.[39] The oxidation of S^{2-} of WS_4^{2-} anions and simultaneous reduction of W^{6+} to W^{4+} occur in this temperature region to form the WS_2 phase.[40,41] However, partial decomposition or redeposition of the S^{2-} species cannot fully reduce the W^{6+} species, resulting in the existence of the WS_3 phase.[41] Due to the decomposition and subsequent redeposition of the sulfur component, the weight suddenly

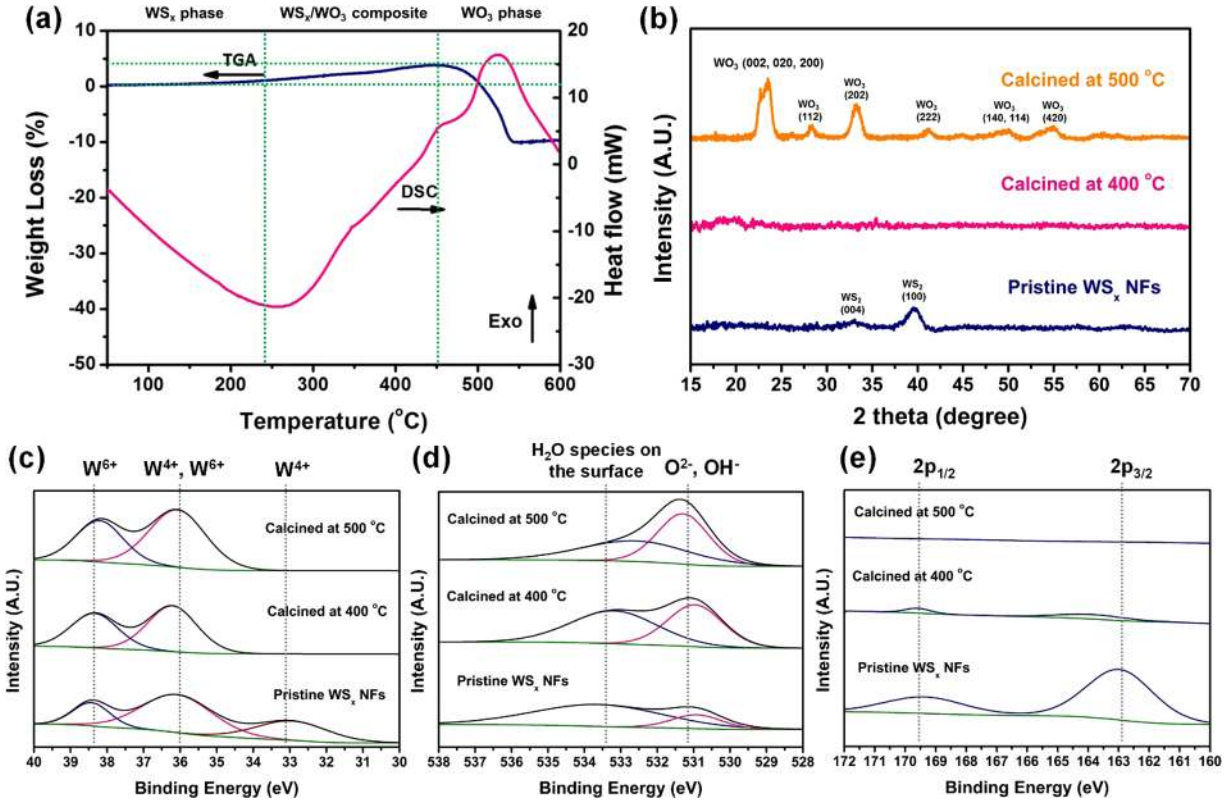

Figure 3. (a) Thermogravimetric analysis (TGA) and differential scanning calorimetry (DSC) curves of WS_x nanofibers with increasing temperature in air; (b) X-ray diffraction (XRD) patterns of the pristine and calcined WS_x nanofibers at 400 and 500 °C; X-ray photoelectron spectra obtained from the pristine and calcined WS_x nanofibers at 400 and 500 °C collected in the (c) W 4f, (d) O 1s, and (e) S 2p.

decreases over 140 °C and is then reversely recovered at 216 °C in the TGA curve. The second endothermic peak at 400 °C corresponds to the decomposition of the SAN polymers.[42] After the decomposition of the SAN, the weight of the NFs was stably maintained, indicating that there is no further decomposition reaction. We conducted the second thermal treatment of the WS_x NFs in air to form an oxide surface that would protect against sulfur dissolution during cell operation. We show the thermal behavior of WS_x NFs with increasing heating temperature in air (Figure 3a). We observe no weight difference below 240 °C. However, a slight weight gain (~5 wt %) is observed from 240 to 450 °C, which corresponds to the growth of thorns on the sulfide surfaces. We notice a sudden weight loss of 10 wt % and an exothermic peak begins at 450 °C, indicating a phase conversion reaction of sulfides to oxides.[43−45]

Structural Features and Phase Information. X-ray diffraction (XRD) patterns of the pristine and calcined NFs to identify the crystal structure are shown in Figure 3b. The pristine WS_x NFs show broad WS_2 peaks related to weak crystallinity. The peaks disappear after calcination in air, indicating amorphous WS_x/WO_3 phases. We observe peaks corresponding to a WO_3 phase after calcination at 500 °C. We also conducted Raman spectroscopy to confirm the atomic vibration mode in the samples (Figure S4). The pristine WS_x NFs show small Raman peaks related to a weakly crystalline WS_2 domain. The peaks disappear after calcination at 400 °C in air. The absence of Raman spectra is known as the typical feature of an amorphous sulfide structure because the S−W−S stretching mode is weakened in the case of the amorphous phase.[41] The peaks corresponding to a WO_3 phase are shown after calcination at 500 °C. The tendency of the Raman results fully match the XRD results. To further identify the crystalline structure, X-ray photoelectron spectroscopy (XPS) was performed for the NF samples prepared at different heating temperatures. We present XPS peaks of NF surfaces collected in the W 4f region. Three different peaks are shown at 33, 36, and 38.5 eV, corresponding to W^{4+}, $W^{4+,6+}$, and W^{6+}, respectively (Figure 3c).[46,47] This result verifies that the NFs obtained after the first calcination show the mixed phases of WS_2 (W^{4+}) and WS_3 (W^{6+}). After calcination in air, the peak related to W^{4+} is diminished, verifying that the WS_2 phase disappears from the surface. From the XPS data collected in the O 1s and S 2p regions, the peak density related to the oxide phase near 531 eV in O 1s increases, and peaks related to the sulfur phase in S 2p disappear at the same time (Figure 3d and e). This observation supports the conclusion that the oxide surface layer is formed on the sulfide NF backbone by post-thermal treatment in air. An oxysulfide intermediate phase could be formed by the calcination process in air as a result of oxygen diffusion into the sulfide structure.[48−51] However, this reaction may occur quickly, and we could not find any residual oxysulfide phase in the samples.[49,50] For the O 1s region, features related to H_2O and oxide (or hydroxide) result from minor surface contamination by limited exposure to ambient air for *ex-situ* characterizations (Figure 3d).[52] Because there is no oxygen content in the pristine WS_x nanofiber, the contamination peak becomes relatively higher than the W−O peak (~531 eV) before post-thermal treatment.

TEM Analysis. To elucidate the crystalline structure and phase information in more detail, we show transmission electron microscopy (TEM) images of the pristine WS_x and

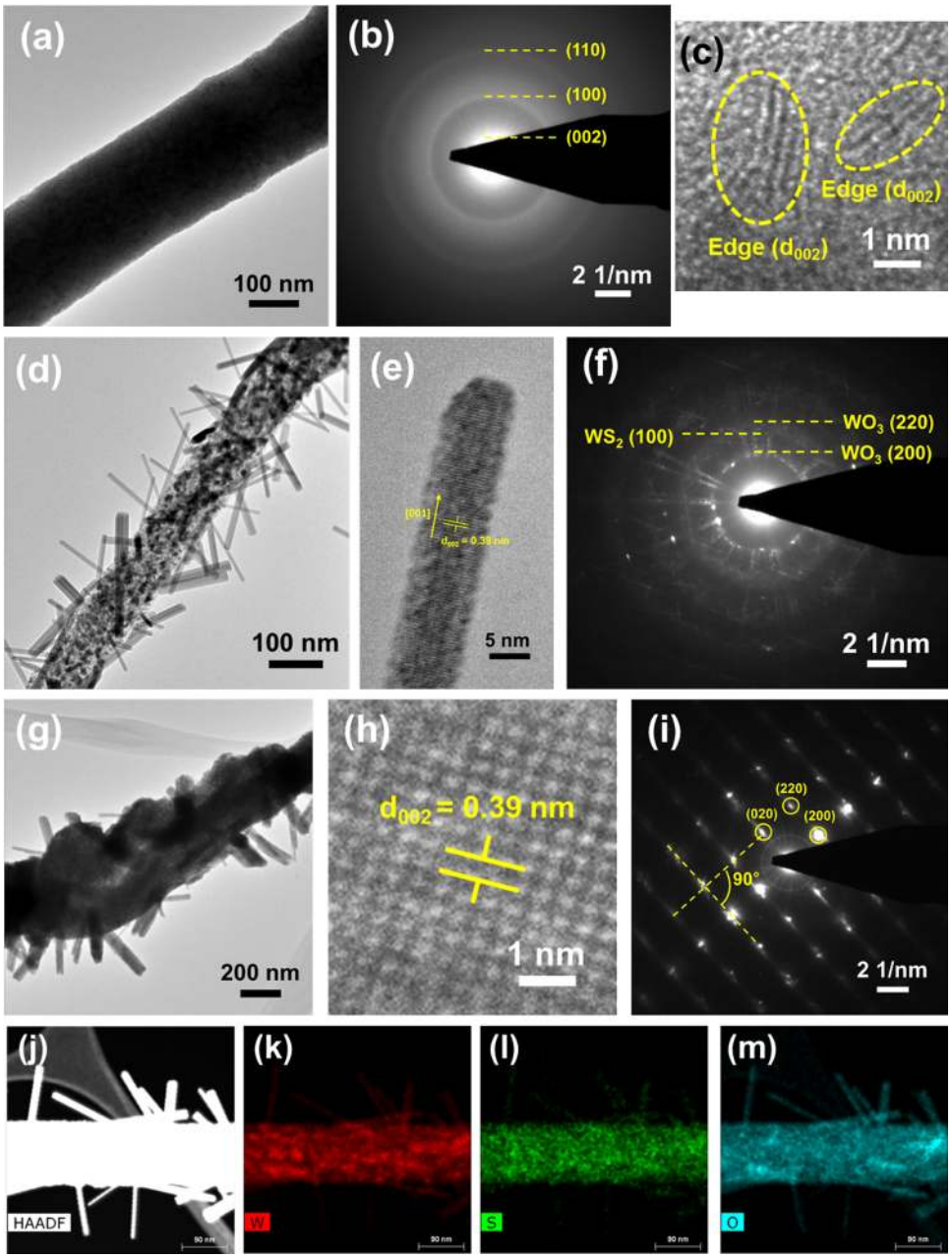

Figure 4. (a) TEM image, (b) SAED patterns, and (c) lattice fringe of WS_x nanofibers calcined at 700 °C for 6 h under a reducing atmosphere (H_2/N_2, 10%/90% v/v); (d, e) TEM images and (f) SAED patterns of postcalcined WS_x nanofibers at 400 °C in air; (g) TEM image, (h) lattice fringe, and (i) SAED patterns of WS_x nanofibers postcalcined at 500 °C in air; (j) HAADF image of postcalcined WS_x nanofibers at 400 °C in air and element maps of (k) tungsten, (l) sulfur, and (m) oxygen.

heterogeneous WS_x/WO_3 NFs (Figure 4). The single WS_x NF shown has a uniform and dense microstructure with a diameter of approximately 200 nm, similar to the scanning electron microscopy (SEM) observations (Figure 4a). Selected area electron diffraction (SAED) patterns are blurred, but likely relate to the WS_2 phase, which is consistent with the XRD results (Figure 4b). From the magnified image, we find nanocrystallite (3−5 layers) and d_{002} edges of the WS_2 phase (Figure 4c).[29] Outside of these regions, we notice the amorphous features related to the WS_3 phase. From energy dispersive spectroscopy (EDS) analysis, the atomic ratio of sulfur/tungsten is 2.82, indicating that WS_2:WS_3 is approximately 2:8 in the WS_x NFs. After calcination at 400 °C, we observe random growth of numerable nanothorns along the vertical direction of the NFs. The average length and diameter of the thorns are 100 and 10 nm, respectively (Figure 4d). The interplanar spacing of the thorns is 0.39 nm, which corresponds to the (002) plane of the WO_3 phase (JCPDS no. 43-1035, Figure 4e).[53] The thorn part exhibits a long-range-ordered crystal lattice along the axial [001] direction as a single-crystalline structure. From the SAED patterns, ring patterns of the WO_3 phase were mainly found and the WS_2 phase becomes blurry, indicating that the sulfide phases are oxidized on the surface and turn into WO_3 phases with a thorn structure (Figure 4f). The split signals around the ring patterns of the WO_3 present the typical feature of randomly aligned nanothorn structures because the transmitting electron beam is diffracted into random directions near the bunch of nanothorns. We

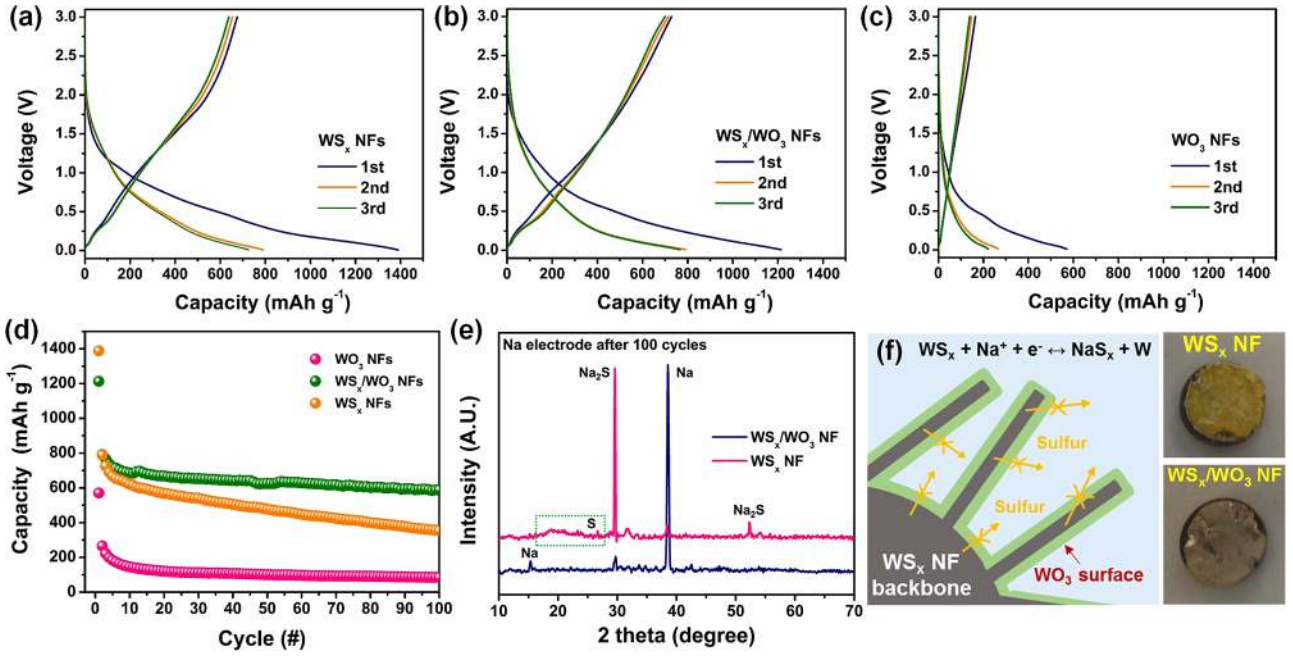

Figure 5. Charge/discharge voltage curves of (a) the pristine WS_x nanofibers and the postcalcined WS_x nanofibers at (b) 400 and (c) 500 °C during the initial three cycles. The electrochemical experiments were carried out at a current density of 100 mA g^{-1}; (d) cycle performance of the WS_x nanofibers and the postcalcined WS_x nanofibers at 400 and 500 °C in a voltage window between 3.0 and 0.01 V at a current density of 100 mA g^{-1}; (e) *ex-situ* XRD patterns of the Na counter electrode after 100 cycles collected from the cells utilizing WS_x and WS_x/WO_3 nanofiber electrodes; (f) schematic illustration of the reaction mechanism during cell operation and photos of Na counter electrodes.

reveal the TEM image of a NF calcined at 500 °C (Figure 4g). WO_3 grains were formed throughout the NF, resulting from the phase conversion reaction corresponding to the TGA/DSC results (Figure 3a). We notice that the nanothorns become shortened and particles undergo grain growth in the NFs, similar to the SEM observations (Figures 2f and i). The interplanar distance of the NFs calcined at 500 °C was approximately 0.39 nm, which corresponds to the (002) plane of the crystalline WO_3 phase (JCPDS no. 43-1035, Figure 4h). SAED patterns show the monoclinic characteristics of (020), (220), and (200) planes with an angle of 90°, which correspond to the typical WO_3 crystalline structure (Figure 4i).[53] Amorphous WS_3 phase and WS_2 nanodomains are not identified in SAED patterns. Therefore, to substantiate our argument that the WO_3 and WS_x phases coexist in the thorn-bush NFs after thermal treatment at 400 °C, we present transmission electron microscopy–energy dispersive spectroscopy (TEM-EDS) elemental mapping carried out using high-angle annular dark-field (HAADF) imaging (Figure 4j–m). We show that all the W, S, and O species are uniformly distributed throughout the fibers. We note that sulfur is observed in the thorn part as well as the stem, identifying that the amorphous WS_x phase exists as a core part hyperbranched structure (Figure 4l). These observations show that the hierarchical NF structure composed of heterogeneous WS_x (core) and WO_3 (shell) was successfully synthesized by simple electrospinning and subsequent thermal treatment control without using complex synthesis procedures.

Electrochemical Properties. The electrochemical performance of the heterogeneous thorn-bush NFs was evaluated to assess their potential as an alternative anode material in a Na-ion cell. We present the charge–discharge profiles of WS_x NFs, WS_x/WO_3 NFs, and WO_3 NFs, corresponding to pristine, postcalcined at 400 °C, and postcalcined at 500 °C, respectively (Figure 5a–c). The Na insertion/extraction reactions occur *via* (i) formation of Na_2S and metal nanoparticles from metal sulfides for discharging and (ii) reversible reconstruction to the original phase from the products for charging.[26] The WS_x phase involves two different metal sulfides composed of amorphous WS_3 and crystalline WS_2. Each WS_3 and WS_2 phase reacts with Na to form the sodium sulfide (Na_2S) and W^0 phases corresponding to the following reactions:

$$WS_3 + 6Na^+ + 6e^- \rightarrow 3Na_2S + W \quad (\text{for } WS_3)$$

$$WS_2 + 4Na^+ + 4e^- \rightarrow 2Na_2S + W \quad (\text{for } WS_2)$$

We show charge–discharge curves of the WS_x NF sample for the first, second, and third cycles between 3.0 and 0.01 V at a current density of 100 mAh g^{-1} (Figure 5a). The sloping charge and discharge curves shown are typical of voltage curves of a reversible conversion reaction.[34,54,55] Unlike crystalline metal disulfides (*e.g.*, MoS_2, WS_2),[26,30,31] the WS_x NFs did not show a distinct plateau at the high voltage region above 1.0 V, indicating that a one-phase reaction occurs at the beginning of discharge instead of a typical two-phase intercalation reaction.[26,28,56] Na ions were inserted into a substantial portion of the amorphous WS_3 phase in the WS_x NFs, and a one-phase reaction ($WS_3 + Na^+ + e^- \rightarrow NaWS_3$) was exhibited prior to the subsequent conversion reaction. The sloping feature of the discharge curves is also associated with a nanosize effect of the sulfide anodes. Although partially crystalline, the WS_2 portions are discretely dispersed in the WS_x NFs. Nanocrystallites of WS_2 with 3–5 layers (less than 5 nm) offer a reduced miscibility gap, resulting in the absence of a two-phase reaction due to the shortened intercalation pathway. Therefore, the sloping feature of WS_x NFs in terms of the one-phase reaction characteristics likely originates from the amorphous WS_3 and nanocrystalline WS_2 phases. We show that even after oxide

formation on the surface of the WS_x NFs (WS_x/WO_3 NFs) the profiles are similar, verifying that there is negligible phase change of sulfide backbone as the main active material (Figure 5b). Although WO_3 NF samples obtained after 500 °C heat treatment in air also show sloping features indicating a conversion reaction ($WO_3 + 6Na^+ + 6e^- \leftrightarrow 3Na_2O + W$),[30] the capacity decreases sharply, dropping below 300 mAh g^{-1} after the second cycle (Figure 5c). This sudden decrease is due to insufficient Na capability into the oxide structure, which corresponds to the typically low capacity of oxide materials.

The WS_x NFs delivered an initial discharge capacity of 1389 mAh g^{-1} and a second discharge capacity of 790 mAh g^{-1}, indicating that the irreversible capacity loss is 599 mAh g^{-1} and is mainly related to the solid electrolyte interface (SEI) formation on the electrode surface. On the other hand, the WS_x/WO_3 NFs exhibit a lower initial discharge capacity (1213 mAh g^{-1}) and a nearly identical second discharge capacity (791 mAh g^{-1}). Although the theoretical capacities of WS_2 and WS_3 are estimated as 574 and 432 mAh g^{-1}, respectively, nanostructured conversion reaction anodes with large surface area often exceed their theoretical values due to (i) reversible decomposition of the electrolyte as a side reaction associated with the formation of an SEI layer and (ii) extra Na^+ adsorption−desorption on the SEI corresponding to interfacial storage.[23,26,57] The decreased irreversible capacity loss demonstrates that the oxide surface layer also stabilizes the SEI formation and prevents substantial growth of an SEI layer. By wrapping or surrounding the active material surface with stable materials, which occurs when the SEI layer growth is stabilized, the amount of irreversible capacity loss can be lowered.[58,59] The stable WO_3 surface helps to prevent direct contact between the sulfide and the electrolyte and relieve vigorous SEI formation as a function of irreversible capacity value. The consistency of the second discharge capacity between the WS_x NFs and the WS_x/WO_3 NFs suggests that the sulfide portion was not much reduced in the reaction that formed the thorn-structured oxides.

The rate capabilities of the samples were examined at different current densities ranging from 100 to 1000 mA g^{-1} (Figure S6). The WS_x NFs deliver a high specific discharge capacity of 500 mAh g^{-1} (70% of the discharge capacity at 100 mA g^{-1}) even at a high current density of 1000 mA g^{-1} (Figure S6a and d). Interestingly, the protective WO_3 surface layer on the WS_x/WO_3 NFs does not impede the rate capability at the high current density of 1000 mA g^{-1} (68% of the discharge capacity at 100 mA g^{-1}) compared to the pristine WS_x NFs (Figure S6a, b, and d). The extended surface area of the thorn-bush NFs as a result of nanobranch formation provides more reaction sites for Na ions, and the thin layer of WO_3 on the WS_x NF backbone can effectively maintain the kinetic performance. On the other hand, the WO_3 NFs show a low capacity value below 250 mA g^{-1} at 100 mA g^{-1} and a poor rate capability value at 1000 mA g^{-1} (19% of the discharge capacity at 100 mA g^{-1}) (Figure S6c and d). This result suggests that the sulfide structure offers better Na reaction kinetics in a conversion reaction than the oxide structure.

To demonstrate the effects of the oxidation treatment on the cycle performance in a Na-ion cell, we present discharge capacity *vs* increasing cycle number for the WO_3, WS_x/WO_3, and WS_x NF materials (Figure 5d). While the WS_x NFs show a high second discharge capacity, the capacity degrades continuously during cycling. For the post-heat-treated WS_x/WO_3 NFs, 74% of the second discharge capacity was maintained after 100 cycles, compared to 44% retention for the pristine WS_x NF electrodes. On the other hand, WO_3 NFs obtained from the oxide conversion at 500 °C delivered a capacity below 100 mAh g^{-1} after 100 cycles. The WO_3 surface on the WS_x NFs contributes to the capacity value by its own conversion reaction. However, the main portion of the capacity of the WS_x/WO_3 NFs comes from the WS_x NF stem. The WO_3 surface mainly plays a role as a coating layer to prevent sulfur dissolution, thereby improving the cycle performance.

***Ex-Situ* Characterizations.** To support the conclusion that the functional oxide coating achieved by this simple thermal treatment in air helps to restrict the intermediate sulfur dissolution during the conversion reaction, we examined a Na counter electrode that had undergone 100 cycles. We show the *ex-situ* XRD patterns of a Na counter electrode obtained from disassembly of a Na-ion cell comprising WS_x and WS_x/WO_3 NF electrodes, respectively (Figure 5e). In the case of the WS_x NFs, the main peaks for Na_2S and subpeaks for sulfur phases were found, verifying that sulfur dissolution eventually occurred during cell operation and that the sulfur components were deposited on the Na counter electrode. The peaks related to Na_2S correspond to the cubic Li_2S phase with the space group *Fm*3*m*.[60] In the case of the Na counter electrode opposite the WS_x/WO_3 NFs, sharp peaks related to Na were observed at 38.6° (indexed based on a body-centered cubic structure), and the Na_2S peaks are significantly diminished, with an absence of sulfur peaks. We show images of the cycled Na counter electrodes obtained from the cells employing WS_x and WS_x/WO_3 NF electrodes, respectively (Figure 5f). While the Na electrode for the WS_x NF cell appears yellow in color, which is typical of sulfur components, there was no significant appearance of yellow on the Na electrode for the WS_x/WO_3 NF sample. These results confirm that modifying a WS_x NF electrode with an oxide surface layer effectively alleviates sulfur dissolution. High capacity and improved cycle performance of Na-ion battery anodes can be simultaneously achieved by the introduction of hierarchical sulfide NF materials with oxide surface features.

CONCLUSION

In summary, we report on heterogeneous tungsten sulfide-oxide (core−shell) NF materials with thorn-bush features and excellent anode performance for high-capacity, long-cycle Na-ion batteries. We successfully synthesized mixed sulfide structures, composed of amorphous WS_3 and crystalline WS_2 phases, *via* electrospinning of $(NH_4)_2WS_4$/SAN composite fibers and subsequent calcination under a reducing atmosphere. To prevent sulfur dissolution during the conversion reaction of sulfides in a Na-ion cell using such an anode, post-thermal treatment in air for a short time (~10 min) is conducted to form an oxide passivation layer. Interestingly, randomly aligned thorns are grown on WS_x NFs as a hierarchical structure, affording more reaction sites for Na ions. The morphological and structural evolutions of the NF material during post-thermal treatment are investigated against increasing temperature. The heterogeneous WS_x/WO_3 NF electrodes delivered a superb second discharge capacity of 791 mA h g^{-1} with reduced irreversible capacity loss and showed improved cycle performance for 100 cycles compared to a pristine WS_x NF electrode. We also substantiate the supposition that an oxide surface on the NFs relieves the expected sulfur dissolution by observing the appearance of sulfur on cycled Na counter electrodes. Our synthesis strategy hints at a simple and functional way to

fabricate heterogeneous sulfide/oxide nanostructures that enable further improvement in battery performance and may find a use in other applications as well.

METHODS

Material Synthesis. Ammonium tetrathiotungstate ($(NH_4)_2WS_4$), styrene acrylonitrile (M_w = 130 000), sulfur, and *N*,*N*-dimethylformamide (99.8%) as precursor chemicals were purchased from Alfa Aesar (Ward Hill, MA, USA). All chemicals were used without further purification. WS_x nanofibers were synthesized by a one-step electrospinning technique using a single nozzle. The precursor solution was prepared by dissolving the $(NH_4)_2WS_4$ (1.607 g) and the SAN (1.7 g) into DMF (8 g) and stirring overnight at 50 °C. The precursor solution was loaded into a syringe with a metal needle, and the electrospinning process was carried out with the following parameters: applied voltage, 20 kV; feeding rate, 10 μL/min; needle size, 23 G; distance between the metal needle and collector, 15 cm; humidity, <10%; temperature, ~30 °C. WS_x NFs were obtained by annealing the as-spun mat at 700 °C for 6 h with a heating rate of 10 °C/min under a reducing atmosphere (H_2/N_2, 10%/90% v/v). SAN was burnt away during the annealing treatment, and the $(NH_4)_2WS_4$ precursor was converted into the WS_x phase composed of WS_2 and WS_3. Post-thermal treatment was conducted at different calcination temperatures for a short time (<10 min) with a heating rate of 10 °C/min in air to form an oxide layer on the WS_x NFs.

Material Characterization. The surface morphology of the samples was analyzed using a scanning electron microscope (Hitachi SU-70). A transmission electron microscope (FEI, Tecnai Osiris at 200 kV) equipped with an energy dispersive spectrometer was used to obtain information on the atomic distributions and internal microstructure of the samples. The crystal structure of the samples was examined by means of X-ray diffraction (Rigaku, D/MAX-RC). A surface analysis to verify the chemical structure of the sulfide and the oxide surface layer after postheat treatment in air was carried out with X-ray photoelectron spectroscopy. XPS measurements were performed at Brookhaven National Laboratory on a Specs Phoibos 100 MCD analyzer under ultra-high-vacuum (2×10^{-10} Torr) conditions. The phase evolution mechanism was elucidated using thermogravimetric analysis (TA Instruments Q50) and differential scanning calorimetry (PerkinElmer DSC7).

Electrochemical Characterization. The electrode was fabricated on copper foil using a casting slurry consisting of 80 wt % active material, 10 wt % carbon (Super-P), and 10 wt % polyvinylidenedifluoride binder in *N*-methyl-2-pyrrolidone. The electrode was then dried under vacuum at 75 °C prior to cell assembly. Half-cells were assembled in an argon-purged glovebox with the prepared electrodes. A Na−metal foil was used as the counter electrode. One molar sodium perchlorate ($NaClO_4$) in polycarbonate and a glass microfiber filter (13 mm diameter, Whatman Co. Ltd.) were used as the electrolyte and the separator, respectively. All of the potentials refer to Na/Na^+. All electrochemical experiments were performed at room temperature.

ASSOCIATED CONTENT

Supporting Information

The Supporting Information is available free of charge on the ACS Publications website at DOI: 10.1021/acsnano.5b06538.

Additional characterization data including SEM images of precursor/polymer composite fibers, morphological evolution of the obtained nanofibers, thermogravimetric analysis and differential scanning calorimetry curves of precursor/polymer composite fibers, Raman spectra, CV curves, rate capability, energy dispersive spectroscopy, and element weight percent data of the Na counter electrode after 100 cycles (PDF)

AUTHOR INFORMATION

Corresponding Author

*E-mail: andre.taylor@yale.edu (André D. Taylor).

Present Address

⊥Department of Chemical and Biological Engineering, Sookmyung Women's University, Seoul, 04310, Republic of Korea (W.-H. Ryu).

Notes

The authors declare no competing financial interest.

ACKNOWLEDGMENTS

W.-H.R. acknowledges support from The NatureNet Program of the Nature Conservancy. The National Science Foundation NSF-CBET-0954985 PECASE Award and MRSEC DMR 1119826 (CRISP) provided partial support of this work. The Yale Institute for Nanoscience and Quantum Engineering (YINQE) and NSF MRSEC DMR 1119826 (CRISP) provided facility support. Research was carried out in part at the Center for Functional Nanomaterials, Brookhaven National Laboratory, which is supported by the U.S. Department of Energy, Office of Basic Energy Sciences, under Contract DE-AC02-98CH10886.

REFERENCES

(1) Dunn, B.; Kamath, H.; Tarascon, J. M. Electrical Energy Storage for the Grid: a Battery of Choices. *Science* **2011**, *334*, 928−935.

(2) Larcher, D.; Tarascon, J. M. Towards Greener and More Sustainable Batteries for Electrical Energy Storage. *Nat. Chem.* **2015**, *7*, 19−29.

(3) Kim, S. W.; Seo, D. H.; Ma, X. H.; Ceder, G.; Kang, K. Electrode Materials for Rechargeable Sodium-Ion Batteries: Potential Alternatives to Current Lithium-Ion Batteries. *Adv. Energy Mater.* **2012**, *2*, 710−721.

(4) Slater, M. D.; Kim, D.; Lee, E.; Johnson, C. S. Sodium-Ion Batteries. *Adv. Funct. Mater.* **2013**, *23*, 947−958.

(5) Ellis, B. L.; Nazar, L. F. Sodium and Sodium-Ion Energy Storage Batteries. *Curr. Opin. Solid State Mater. Sci.* **2012**, *16*, 168−177.

(6) Palomares, V.; Casas-Cabanas, M.; Castillo-Martinez, E.; Han, M. H.; Rojo, T. Update on Na-Based Battery Materials. A Growing Research Path. *Energy Environ. Sci.* **2013**, *6*, 2312−2337.

(7) Yabuuchi, N.; Kubota, K.; Dahbi, M.; Komaba, S. Research Development on Sodium-Ion Batteries. *Chem. Rev.* **2014**, *114*, 11636−11682.

(8) Lim, S. J.; Han, D. W.; Nam, D. H.; Hong, K. S.; Eom, J. Y.; Ryu, W. H.; Kwon, H. S. Structural Enhancement of $Na_3V_2(PO_4)_3$/C Composite Cathode Materials by Pillar Ion Doping for High Power and Long Cycle Life Sodium-Ion Batteries. *J. Mater. Chem. A* **2014**, *2*, 19623−19632.

(9) Doeff, M. M.; Ma, Y. P.; Visco, S. J.; Dejonghe, L. C. Electrochemical Insertion of Sodium into Carbon. *J. Electrochem. Soc.* **1993**, *140*, L169−L170.

(10) Chevrier, V. L.; Ceder, G. Challenges for Na-Ion Negative Electrodes. *J. Electrochem. Soc.* **2011**, *158*, A1011−A1014.

(11) Ponrouch, A.; Goni, A. R.; Palacin, M. R. High Capacity Hard Carbon Anodes for Sodium Ion Batteries in Additive Free Electrolyte. *Electrochem. Commun.* **2013**, *27*, 85−88.

(12) Pol, V. G.; Lee, E.; Zhou, D. H.; Dogan, F.; Calderon-Moreno, J. M.; Johnson, C. S. Spherical Carbon as a New High-Rate Anode for Sodium-Ion Batteries. *Electrochim. Acta* **2014**, *127*, 61−67.

(13) Tang, K.; Fu, L. J.; White, R. J.; Yu, L. H.; Titirici, M. M.; Antonietti, M.; Maier, J. Hollow Carbon Nanospheres with Superior Rate Capability for Sodium-Based Batteries. *Adv. Energy Mater.* **2012**, *2*, 873−877.

(14) Kim, Y.; Kim, Y.; Choi, A.; Woo, S.; Mok, D.; Choi, N. S.; Jung, Y. S.; Ryu, J. H.; Oh, S. M.; Lee, K. T. Tin Phosphide as a Promising

Anode Material for Na-Ion Batteries. *Adv. Mater.* **2014**, *26*, 4139−4144.
(15) Qian, J. F.; Xiong, Y.; Cao, Y. L.; Ai, X. P.; Yang, H. X. Synergistic Na-Storage Reactions in Sn_4P_3 as a High-Capacity, Cycle-stable Anode of Na-Ion Batteries. *Nano Lett.* **2014**, *14*, 1865−1869.
(16) Nam, D. H.; Kim, T. H.; Hong, K. S.; Kwon, H. S. Template-Free Electrochemical Synthesis of Sn Nanofibers as High-Performance Anode Materials for Na-Ion Batteries. *ACS Nano* **2014**, *8*, 11824−11835.
(17) Zhu, H. L.; Jia, Z.; Chen, Y. C.; Weadock, N.; Wan, J. Y.; Vaaland, O.; Han, X. G.; Li, T.; Hu, L. B. Tin Anode for Sodium-Ion Batteries Using Natural Wood Fiber as a Mechanical Buffer and Electrolyte Reservoir. *Nano Lett.* **2013**, *13*, 3093−3100.
(18) Farbod, B.; Cui, K.; Kalisvaart, W. P.; Kupsta, M.; Zahiri, B.; Kohandehghan, A.; Lotfabad, E. M.; Li, Z.; Luber, E. J.; Mitlin, D. Anodes for Sodium Ion Batteries Based on Tin-Germanium-Antimony Alloys. *ACS Nano* **2014**, *8*, 4415−4429.
(19) Xu, Y.; Zhou, M.; Wen, L. Y.; Wang, C. L.; Zhao, H. P.; Mi, Y.; Liang, L. Y.; Fu, Q.; Wu, M. H.; Lei, Y. Highly Ordered Three-Dimensional Ni-TiO_2 Nanoarrays as Sodium Ion Battery Anodes. *Chem. Mater.* **2015**, *27*, 4274−4280.
(20) Wu, L. M.; Bresser, D.; Buchholz, D.; Giffin, G. A.; Castro, C. R.; Ochel, A.; Passerini, S. Unfolding the Mechanism of Sodium Insertion in Anatase TiO_2 Nanoparticles. *Adv. Energy Mater.* **2015**, *5*, 1401142.
(21) Xu, J.; Ma, C. Z.; Balasubramanian, M.; Meng, Y. S. Understanding $Na_2Ti_3O_7$ as an Ultra-Low Voltage Anode Material for a Na-Ion Battery. *Chem. Commun.* **2014**, *50*, 12564−12567.
(22) Klein, F.; Jache, B.; Bhide, A.; Adelhelm, P. Conversion Reactions for Sodium-Ion Batteries. *Phys. Chem. Chem. Phys.* **2013**, *15*, 15876−15887.
(23) Hu, Y. Y.; Liu, Z.; Nam, K. W.; Borkiewicz, O. J.; Cheng, J.; Hua, X.; Dunstan, M. T.; Yu, X.; Wiaderek, K. M.; Du, L. S.; et al. Origin of Additional Capacities in Metal Oxide Lithium-Ion Battery Electrodes. *Nat. Mater.* **2013**, *12*, 1130−1136.
(24) Hasa, I.; Verrelli, R.; Hassoun, J. Transition Metal Oxide-Carbon Composites as Conversion Anodes for Sodium-Ion Battery. *Electrochim. Acta* **2015**, *173*, 613−618.
(25) Wang, L. P.; Yu, L. H.; Wang, X.; Srinivasan, M.; Xu, Z. C. J. Recent Developments in Electrode Materials for Sodium-Ion Batteries. *J. Mater. Chem. A* **2015**, *3*, 9353−9378.
(26) Ryu, W. H.; Jung, J. W.; Park, K.; Kim, S. J.; Kim, I. D. Vine-Like MoS_2 Anode Materials Self-Assembled from 1-D Nanofibers for High Capacity Sodium Rechargeable Batteries. *Nanoscale* **2014**, *6*, 10975−10981.
(27) Choi, S. H.; Ko, Y. N.; Lee, J. K.; Kang, Y. C. 3D MoS_2-Graphene Microspheres Consisting of Multiple Nanospheres with Superior Sodium Ion Storage Properties. *Adv. Funct. Mater.* **2015**, *25*, 1780−1788.
(28) Wang, X. F.; Shen, X.; Wang, Z. X.; Yu, R. C.; Chen, L. Q. Atomic-Scale Clarification of Structural Transition of MoS_2 upon Sodium Intercalation. *ACS Nano* **2014**, *8*, 11394−11400.
(29) Su, D. W.; Dou, S. X.; Wang, G. X. WS_2@Graphene Nanocomposites as Anode Materials for Na-Ion Batteries with Enhanced Electrochemical Performances. *Chem. Commun.* **2014**, *50*, 4192−4195.
(30) Choi, S. H.; Kang, Y. C. Sodium Ion Storage Properties of WS_2-Decorated Three-Dimensional Reduced Graphene Oxide Microspheres. *Nanoscale* **2015**, *7*, 3965−3970.
(31) Hu, Z.; Wang, L. X.; Zhang, K.; Wang, J. B.; Cheng, F. Y.; Tao, Z. L.; Chen, J. MoS_2 Nanoflowers with Expanded Interlayers as High-Performance Anodes for Sodium-Ion Batteries. *Angew. Chem., Int. Ed.* **2014**, *53*, 12794−12798.
(32) Matsuyama, T.; Hayashi, A.; Ozaki, T.; Mori, S.; Tatsumisago, M. Electrochemical Properties of All-Solid-State Lithium Batteries with Amorphous MoS_3 Electrodes Prepared by Mechanical Milling. *J. Mater. Chem. A* **2015**, *3*, 14142−14147.
(33) David, L.; Bhandavat, R.; Singh, G. MoS_2/Graphene Composite Paper for Sodium-Ion Battery Electrodes. *ACS Nano* **2014**, *8*, 1759−1770.
(34) Wang, J. J.; Luo, C.; Gao, T.; Langrock, A.; Mignerey, A. C.; Wang, C. S. An Advanced MoS_2/Carbon Anode for High-Performance Sodium-Ion Batteries. *Small* **2015**, *11*, 473−481.
(35) Ahmed, B.; Anjum, D. H.; Hedhili, M. N.; Alshareef, H. N. Mechanistic Insight into the Stability of HfO_2-Coated MoS_2 Nanosheet Anodes for Sodium Ion Batteries. *Small* **2015**, *11*, 4341−4350.
(36) Ji, X. L.; Lee, K. T.; Nazar, L. F. A Highly Ordered Nanostructured Carbon-Sulphur Cathode for Lithium-Sulphur Batteries. *Nat. Mater.* **2009**, *8*, 500−506.
(37) Manthiram, A.; Fu, Y. Z.; Chung, S. H.; Zu, C. X.; Su, Y. S. Rechargeable Lithium-Sulfur Batteries. *Chem. Rev.* **2014**, *114*, 11751−11787.
(38) Zheng, G. Y.; Yang, Y.; Cha, J. J.; Hong, S. S.; Cui, Y. Hollow Carbon Nanofiber-Encapsulated Sulfur Cathodes for High Specific Capacity Rechargeable Lithium Batteries. *Nano Lett.* **2011**, *11*, 4462−4467.
(39) Prasad, T. P.; Diemann, E.; Muller, A. Thermal-Decomposition of $(NH_4)_2MoO_2S_2$, $(NH_4)_2MoS_4$, $(NH_4)_2WO_2S_2$ and $(NH_4)_2WS_4$. *J. Inorg. Nucl. Chem.* **1973**, *35*, 1895−1904.
(40) Weber, T.; Muijsers, J. C.; Niemantsverdriet, J. W. Structure of Amorphous MoS_3. *J. Phys. Chem.* **1995**, *99*, 9194−9200.
(41) Shi, Y. M.; Wang, Y.; Wong, J. I.; Tan, A. Y. S.; Hsu, C. L.; Li, L. J.; Lu, Y. C.; Yang, H. Y. Self-Assembly of Hierarchical MoS_x/CNT Nanocomposites ($2 < x < 3$): Towards High Performance Anode Materials for Lithium Ion Batteries. *Sci. Rep.* **2013**, *3*, 2169.
(42) Suzuki, M.; Wilkie, C. A. The Thermal-Degradation of Acrylonitrile-Butadiene-Styrene Terpolymer as Studied by Tga/Ftir. *Polym. Degrad. Stab.* **1995**, *47*, 217−221.
(43) Taha, A. A.; Li, F. T. Porous WO_3-Carbon Nanofibers: High-Performance and Recyclable Visible Light Photocatalysis. *Catal. Sci. Technol.* **2014**, *4*, 3601−3605.
(44) Choi, S. J.; Choi, C.; Kim, S. J.; Cho, H. J.; Hakim, M.; Jeon, S.; Kim, I. D. Highly Efficient Electronic Sensitization of Non-oxidized Graphene Flakes on Controlled Pore-loaded WO_3 Nanofibers for Selective Detection of H_2S Molecules. *Sci. Rep.* **2015**, *5*, 8067.
(45) Yu, S.; Jung, J. W.; Kim, I. D. Single Layers of WS_2 Nanoplates Embedded in Nitrogen-Doped Carbon Nanofibers as Anode Materials for Lithium-Ion Batteries. *Nanoscale* **2015**, *7*, 11945−11950.
(46) Mao, X. Z.; Xu, Y.; Xue, Q. X.; Wang, W. X.; Gao, D. Q. Ferromagnetism in Exfoliated Tungsten Disulfide Nanosheets. *Nanoscale Res. Lett.* **2013**, *8*, 430.
(47) Avsar, A.; Tan, J. Y.; Taychatanapat, T.; Balakrishnan, J.; Koon, G. K. W.; Yeo, Y.; Lahiri, J.; Carvalho, A.; Rodin, A. S.; O'Farrell, E. C. T.; et al. Spin-Orbit Proximity Effect in Graphene. *Nat. Commun.* **2014**, *5*, 4875.
(48) Martin-Litas, I.; Vinatier, P.; Levasseur, A.; Dupin, J. C. Characterisation of R.F. Sputtered Tungsten Disulfide and Oxysulfide Thin Films. *Thin Solid Films* **2002**, *416*, 1−9.
(49) Dupin, J. C.; Gonbeau, D.; Martin-Litas, I.; Vinatier, P.; Levasseur, A. Amorphous Oxysulfide Thin Films MO_yS_z (M = W, Mo, Ti) XPS Characterization: Structural and Electronic Pecularities. *Appl. Surf. Sci.* **2001**, *173*, 140−150.
(50) Martinez, H.; Benayad, A.; Gonbeau, D.; Vinatier, P.; Pecquenard, B.; Levasseur, A. Influence of The Cation Nature of High Sulfur Content Oxysulfide Thin Films MO_yS_z (M = W, Ti) Studied by XPS. *Appl. Surf. Sci.* **2004**, *236*, 377−386.
(51) Morrish, R.; Haak, T.; Wolden, C. A. Low-Temperature Synthesis of n-Type WS_2 Thin Films via H_2S Plasma Sulfurization of WO_3. *Chem. Mater.* **2014**, *26*, 3986−3992.
(52) Casalongue, H. S.; Kaya, S.; Viswanathan, V.; Miller, D. J.; Friebel, D.; Hansen, H. A.; Norskov, J. K.; Nilsson, A.; Ogasawara, H. Direct Observation of the Oxygenated Species during Oxygen Reduction on a Platinum Fuel Cell Cathode. *Nat. Commun.* **2013**, *4*, 2817.

(53) Choi, S. J.; Lee, I.; Jang, B. H.; Youn, D. Y.; Ryu, W. H.; Park, C. O.; Kim, I. D. Selective Diagnosis of Diabetes Using Pt-Functionalized WO_3 Hemitube Networks As a Sensing Layer of Acetone in Exhaled Breath. *Anal. Chem.* **2013**, *85*, 1792−1796.
(54) Xu, X.; Fan, Z. Y.; Yu, X. Y.; Ding, S. J.; Yu, D. M.; Lou, X. W. A Nanosheets-on-Channel Architecture Constructed from MoS_2 and CMK-3 for High-Capacity and Long-Cycle-Life Lithium Storage. *Adv. Energy Mater.* **2014**, *4*, 1400902.
(55) Ryu, W. H.; Shin, J.; Jung, J. W.; Kim, I. D. Cobalt(II) Monoxide Nanoparticles Embedded in Porous Carbon Nanofibers as a Highly Reversible Conversion Reaction Anode for Li-Ion Batteries. *J. Mater. Chem. A* **2013**, *1*, 3239−3243.
(56) Park, J.; Kim, J. S.; Park, J. W.; Nam, T. H.; Kim, K. W.; Ahn, J. H.; Wang, G.; Ahn, H. J. Discharge Mechanism of MoS_2 for Sodium Ion Battery: Electrochemical Measurements and Characterization. *Electrochim. Acta* **2013**, *92*, 427−432.
(57) Cabana, J.; Monconduit, L.; Larcher, D.; Palacin, M. R. Beyond Intercalation-Based Li-Ion Batteries: The State of the Art and Challenges of Electrode Materials Reacting Through Conversion Reactions. *Adv. Mater.* **2010**, *22*, E170−E192.
(58) Wu, H.; Chan, G.; Choi, J. W.; Ryu, I.; Yao, Y.; McDowell, M. T.; Lee, S. W.; Jackson, A.; Yang, Y.; Hu, L. B.; et al. Stable cycling of double-walled silicon nanotube battery anodes through solid-electrolyte interphase control. *Nat. Nanotechnol.* **2012**, *7*, 309−314.
(59) Shin, J.; Park, K.; Ryu, W. H.; Jung, J. W.; Kim, I. D. Graphene Wrapping as a Protective Clamping Layer Anchored to Carbon Nanofibers Encapsulating Si Nanoparticles for a Li-Ion Battery Anode. *Nanoscale* **2014**, *6*, 12718−12726.
(60) Nagao, M.; Hayashi, A.; Tatsumisago, M. High-Capacity Li_2S-Nanocarbon Composite Electrode for All-Solid-State Rechargeable Lithium Batteries. *J. Mater. Chem.* **2012**, *22*, 10015−10020.